RESEARCH ARTICLE

Spectral energy balance in dry convective boundary layers

James Sandham[a][*] and Michael L. Waite[a]

[a]*Department of Applied Mathematics, University of Waterloo, 200 University Ave W, Waterloo, ON N2L 3G1*;

(*June 2014*)

Three-dimensional large-eddy simulations of the convective boundary layer over a domain of approximately 6 km are performed with the UCLA LES model. Simulations are forced with a constant surface heat flux and prescribed subsidence, and are run to equilibrium. Sub-grid scale fluxes are parameterized with the Smagorinsky-Lilly scheme. A range of grid spacings from 40 down to 5 m are employed. Kinetic energy spectra and the various terms in the kinetic energy spectral budget - heat flux, nonlinear transfer, pressure, and dissipation - are computed using two-dimensional discrete Fourier transforms at every vertical level. Despite the fact that isotropic grid spacings of down to 5 m (grid sizes of $1152^2 \times 400$) were used, an inertial range with a -5/3 spectrum is not obtained. Rather, shallower energy spectral slopes that are closer to -4/3 are found. The shallower spectra are shown to possibly result from the injection of kinetic energy over a wide range of scales via a very broad heat flux spectrum. Only with the highest resolution ($\Delta x = 5$ m) does the total heat flux begin to converge and the possibility of local isotropy emerge at small scales. Dependence on surface heat flux and domain size is considered. Preliminary subgrid-scale sensitivity results are obtained through comparison with the turbulent kinetic energy subgrid-scale model.

Keywords: Atmospheric Turbulence, Large Eddy Simulation, Turbulent boundary layers, Turbulent Convection

1. Introduction

In this paper we examine the spectral kinetic energy budget of an atmospheric dry convective boundary layer (CBL) flow using large-eddy simulations (LES). While the heat flux spectrum, which is the main source of kinetic energy (KE) in the CBL, has been considered in several studies [e.g. [1] (observational), [2] (LES), [3] (wind tunnel)], the remaining terms in the spectral budget have received less attention. We investigate the budget here to better understand the resulting form of the KE spectrum, and more broadly, the extent to which CBL turbulence exhibits a turbulent inertial range.

Extensive progress has been made in the field of atmospheric LES beginning with the pioneering work of Lilly [4] and Deardorff [5, 6]. Lilly [4] extended the Smagorinsky eddy viscosity model [7] to include convection and performed one of the first three-dimensional LES experiments [8]. Throughout the early 1970's, Deardorff used different techniques to parameterize the sub-grid scale (SGS) fluxes in a CBL, including the Smagorinsky model [6] and the turbulent kinetic energy (TKE) model [9]. Key differences were found between CBLs simulated with these two SGS models. For example, the Smagorinsky model tended to smooth out gradients in the entrainment zone more than the TKE model. Deardorff [5] found

---

[*]Corresponding author. Email: jsandham@uwaterloo.ca

that for flows dominated by thermal convection, a Smagorinsky coefficient near $C_s = 0.21$ is appropriate, while for flows dominated by shear a lower Smagorinsky coefficient around $C_s = 0.13$ should be used.

The boundary layer kinetic energy budget was measured in physical space by Moeng [10]. In the spectral domain, kinetic energy spectra in the CBL have been found to have a $-5/3$ slope (e.g. [11–14]). This spectral slope is a necessary condition of isotropic turbulence, and local isotropy has been investigated by considering the spectral ratio of one-dimensional vertical-to-horizontal (transverse to longitudinal) kinetic energy, which should be $4/3$ in isotropic turbulence [15]. Deardorff [5] found ratios that were much larger than this value as did the subsequent studies of Mestayer [16], Moeng & Wyngaard [13], and Schmidt & Schumann [2]. It seems that the pressure perturbations are only strong enough to encourage local isotropy at the smallest scales. Indeed, the more recent wind tunnel experiments [3] have since found ratios that are very close to the theoretical value (only slightly larger).

The heat flux spectrum is an important term in the spectral KE budget, as it corresponds to a source of KE from buoyant production. Results from the LES experiments of Schmidt & Schumann [2] and the observational study of Kaimal et al. [1] indicate that near the surface heat is transported up by small scale turbulent motions followed by a rapid transfer to larger scales throughout the mixing layer. Significantly, heat appears to be transported within the entrainment region predominantly by the large scale turbulent motions and not small scales as is the case near the surface. Similar results were seen in the wind tunnel experiments of Kiaser & Fedorovich [3] throughout the CBL except near the surface where the experiments showed large scale heat transport which was attributed to surface shear effects.

Observational studies have been performed by many authors (e.g. [1, 17–20]), and these findings have been very useful for validating numerical results. Good agreement has been found between observed and simulated KE and heat flux spectra (for example comparing the computed LES heat flux spectra of Schmidt & Schumann [2] with the observed spectra of Kaimal et al. [1]). Large-scale peaks in the heat flux and kinetic energy spectra have been seen in some studies, possibly caused by coherent structures in the flow [20]. The LES work of Schmidt & Schumann [2] found similar peaks, but caution that the coherent structure interpretation is not universally accepted. For example, Deardorff & Willis' [21] water tank study of CBL did not find statistically significant peaks in the spectra corresponding to coherent structures nor were such peaks observed in the overland aircraft measurements of Lenschow [17].

Numerous comparison studies examining differences in sub-grid scale parameterizations [22–25] and differences between shear and buoyancy driven flows [26] have also been performed. In particular, Niewstadt et al. [22] compared four LES codes that were run with similar domain setups but different parameterizations of the sub-grid scale fluxes. Despite these differences, the LES results showed a high level of agreement in both physical space statistics and kinetic energy spectra. In [25] the standard Smagorinsky-Lilly model was compared with the dynamic Smagorinsky parameterization and similar insensitivities were found. The robustness of LES simulations despite differences in the SGS parameterization is partially due to the inherent large scale eddies that develop in convection driven turbulent flows. It is also encouraging that the LES results are reasonably insensitive to the choice of SGS model as it gives confidence in the use of LES as a tool for studying CBL turbulence.

More recent high-resolution LES of the CBL have examined the effects of grid resolution on physical space statistics and kinetic energy spectra [14]. Resolutions of

up to 1024^3 grid points (corresponding to $5 \times 5 \times 2$ m grid spacings) were employed. Within the mixing layer ($0.1 < z_i < 0.9$, where z_i is the inversion height) the variances and vertical heat flux converged (in physical space) for resolutions of 256^3. However, the temperature variance increased with successive resolutions within the entrainment zone. Both horizontal and vertical velocities showed $-5/3$ spectra, however a two-slope character was observed in the horizontal spectra particularly near the surface and the boundary layer height. It was observed that the horizontal spectra were shallower than $-5/3$ in the larger scales followed by a transition to a $-5/3$ slope within the smaller scales. The peak vertical velocity spectra also shifted to higher wavenumbers as z/z_i decreased.

While the heat flux is an important term in the spectral KE budget, there are other terms - nonlinear transfer and SGS dissipation - which have not been widely studied in the CBL problem (such investigations of the full spectral budget have been performed for larger-scale flows in the atmosphere, e.g Koshyk & Hamilton [27], and ocean, e.g. Capet et al. [28]). In this work, we compute and analyze the full spectral budget in idealized CBL simulations and use it to interpret the form of the KE spectrum. The remainder of this paper is organized as follows. The numerical method and spectral analysis is outlined in section 2. Results are given in section 3, including an overview of the simulations in physical space and investigation of the KE spectra and spectral budget. Sensitivity of results to grid resolution surface heat flow and domain size is assessed and SGS sensitivity is briefly examined. Conclusions are given in section 4.

2.   Methodology

2.1.   *Equations*

We employ the filtered anelastic equations [29]:

$$\frac{\partial \bar{u}_i}{\partial t} = -\bar{u}_j \frac{\partial \bar{u}_i}{\partial x_j} - c_p \Theta_0 \frac{\partial \bar{\pi}'}{\partial x_i} + \frac{\bar{\theta}'}{\Theta_o} g \delta_{i3} + \frac{1}{\rho_o} \frac{\partial (\rho_o \bar{\tau}_{ij})}{\partial x_j},$$

$$\frac{\partial (\rho_o \bar{u}_i)}{\partial x_i} = 0, \qquad (1)$$

$$\frac{\partial \bar{\theta}'}{\partial t} = -\bar{u}_j \frac{\partial \bar{\theta}'}{\partial x_j} + \frac{1}{\rho_0} \frac{\partial (\rho_0 \bar{\gamma}_{\theta j})}{\partial x_j} + \frac{\partial \bar{F}_\theta}{\partial x_j} \delta_{j3} - w_s \frac{\partial \bar{\theta}'}{\partial z},$$

where overbar denotes LES filtering (e.g. Pope [30]), u_i is the velocity, θ' is the potential temperature perturbation about a constant basic state Θ_0, π' is the Exner pressure perturbation function, $\rho_0(z)$ is the basic state density, F_θ is an external forcing such as radiative cooling, and w_s is the subsidence velocity. Since we will be using grid spacings of O(10) m, which is well above the molecular dissipation range, the molecular viscous and diffusion terms are not included. The Coriolis force is neglected. The SGS momentum and temperature fluxes τ_{ij} and $\gamma_{\theta j}$ are closed with [7], [4]:

$$\bar{\tau}_{ij} = -2K_m S_{ij} \quad \text{and} \quad \bar{\gamma}_{\theta j} = -K_h \frac{\partial \bar{\theta}'}{\partial x_j} = -\frac{K_m}{Pr} \frac{\partial \bar{\theta}'}{\partial x_j},$$

where Pr is the Prandtl number, which we take to be $1/3$ [6]; K_m is the eddy

viscosity, which is defined as

$$K_m = (C_s l)^2 |S| \sqrt{\max\left(0, 1 - \frac{Ri}{Pr}\right)},$$

the filtered rate of strain tensor

$$S_{ij} = \frac{1}{2}\left(\frac{\partial \bar{u}_i}{\partial x_j} + \frac{\partial \bar{u}_j}{\partial x_i}\right),$$

and $S^2 = S_{ij}S_{ij}$. The calculation of the Richardson number Ri, is given by:

$$Ri = \frac{N^2}{S^2} \quad, \text{where} \quad N^2 = \frac{g}{\Theta_0}\frac{\partial \bar{\theta}'}{\partial z}.$$

The filter scale, l, is defined as:

$$l = \frac{1}{\sqrt{(\Delta x \Delta y \Delta z)^{-2/3} + (z\kappa/C_s)^{-2}}},$$

where κ is the von Kármán constant. This filter scale approaches zero within the surface layer and $(\Delta x \Delta y \Delta z)^{1/3}$ outside. We choose $C_s = 0.23$ consistent with previous studies [5], [31].

2.2. Numerical Approach

The anelastic equations (1) are integrated with the UCLA LES model [32]. The model uses fourth order centred finite differences for momentum advection and high order upwinded advection for scalars. A MC flux limiter is applied for scalars to ensure that no oscillations occur near sharp gradients. This approach employs a high order spatial discretization for most of the domain, only switching to a lower order scheme when gradients become steep. Time stepping is leapfrog for velocity and forward Euler for scalars, and the time step is never more than 1 s. A variable time step is chosen so that the Courant number remains within the range 0.3 to 0.5. Horizontal boundary conditions are periodic and vertical boundary conditions are discussed below.

The pressure solver exploits horizontal periodicity and uses 2D discrete Fourier transforms. The pressure is found by the projection method [34] which involves applying continuity to the momentum equation:

$$\frac{\partial}{\partial x_i}\left(\rho_0 c_p \Theta_0 \frac{\partial \bar{\pi}'}{\partial x_i}\right) = \left[\frac{\partial}{\partial x_i}\left(-\rho_0 \bar{u}_j \frac{\partial \bar{u}_i}{\partial x_j} + \rho_0 \frac{g\bar{\theta}'}{\Theta_0} + \frac{\partial(\rho_0 \bar{\tau}_{ij})}{\partial x_j}\right)\right]. \tag{2}$$

This results in a one dimensional elliptic equation for every horizontal wave vector,

$$\frac{d^2 \hat{\bar{\pi}}'}{dz^2} - (k^2 + l^2)\hat{\bar{\pi}}' = \hat{f},$$

where $\hat{f}$ is the just the horizontal Fourier transform of the rhs of (2), which is evaluated with a tridiagonal solver.

The code uses a staggered Arakawa-C grid, i.e. all of the velocities are staggered half a grid point in the direction of the velocity component from the thermodynamic points [33]. For example, the w velocities are half a grid point above the thermal points while the u velocities are half a grid point to the right of the thermal points. When necessary, velocities are interpolated to the thermal points using a 4th order interpolation scheme, e.g.

$$w_{j+1/2} = \frac{7}{12}(w_j + w_{j+1}) - \frac{1}{12}(w_{j-1} + w_{j+2}).$$

Vertical boundary conditions are no-normal-flow at the upper and lower boundaries, along with zero Neumann conditions on the scalars and horizontal velocities. These velocity boundary conditions are implemented using ghost points. For example to enforce the Neumann condition on the u velocity we set $u(z = 1) = u(z = 2)$ where $u(z = 1)$ is half a grid point below the surface and $u(z = 2)$ is half a grid point above the surface. In addition, surface fluxes of heat and momentum are imposed at the lower boundary as boundary conditions for the SGS terms. Constant surface temperature fluxes $\bar{\gamma}_{\theta 3}|_{z=0} = Q_s$ are specified, and surface momentum fluxes are parameterized with Monin-Obukhov similarity theory.

All of the simulations are run to 12000 s, with outputs every 1000 s, except for the highest resolution simulation (B5) which is only run to 7500 s with outputs every 500 s. All simulations reach statistical stationarity after approximately 4000 s, and various quantities including the energy spectra and spectral budget terms are averaged from 4000 to 12000 s (7500 in the case of B5). The domain size is $L \times L \times H$, with $n \times n \times m$ grid points. In all simulations, $H = 1990$ m. The initial potential temperature profile is taken from Driel [35], as are the imposed subsidence velocity w_s and radiative cooling (Figure 1).

Three sets of simulations will be presented below (Table 1). The first set explores the base configuration (labeled B in Table 1) and its dependence on resolution. In these simulations, $L = 5750$ m, $Q_s = 0.071$ Km/s, and four grid spacings are considered, with $\Delta z \approx \Delta x = 40$ m, 20 m, 10 m, and 5 m. With this value of surface heat flux and the initial profiles in Figure 1, simulations reached a relatively stationary boundary layer approximately 1000 m in height after around 4000 s. The second set (labeled H in Table 1) investigates the dependence on the surface heat flux: Q_s is doubled to 0.142 Km/s with three different grid spacings. The third set (labeled D in Table 1) explores the dependence on domain size: L is increased to 11500 m and three grid spacings with $20 \leq \Delta x \leq 80$ are employed. For the H experiments with the larger surface heat flux, the initial $\bar{\theta}'_0$ profile is adjusted to be closer to the equilibrium value, but the lapse rate of the free atmosphere is unchanged (Figure 1).

2.3.   *Spectral Budget*

Spectral analysis is performed with 2D discrete Fourier transforms on horizontal planes. The KE per unit volume corresponding to a horizontal wave vector $\vec{k} = (k, l)$ at vertical level z is:

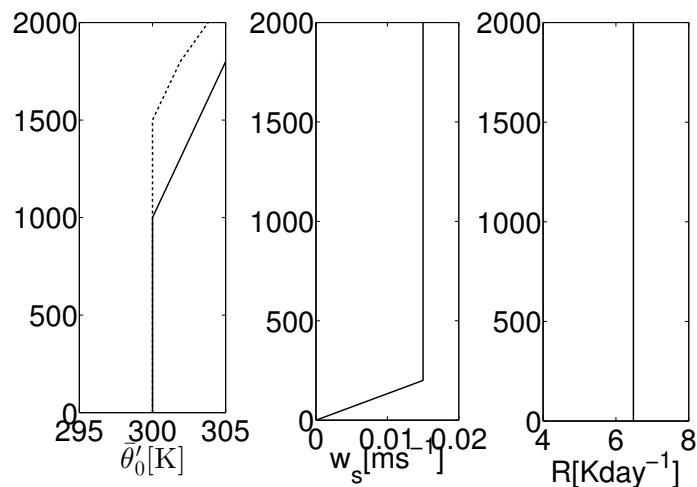$$E(\vec{k}, z, t) = \frac{1}{2}\rho_0 \hat{\bar{u}}_i^*(\vec{k}, z)\hat{\bar{u}}_i(\vec{k}, z),$$

Figure 1.: Initial $\bar{\theta}_0'$, subsidence, and radiative cooling profiles. The dashed line corresponds to experiments with a higher surface heat flux.

where $\hat{}$ denotes horizontal Fourier coefficient, * denotes complex conjugate, and the dependence on t has been suppressed for clarity. The equation for $E(\vec{k}, z)$ can be derived by writing the momentum equation in (1) in the Fourier domain:

$$\frac{\partial \hat{\bar{u}}_i}{\partial t} = -\mathcal{F}[\frac{1}{\rho_0}\frac{\partial}{\partial x_j}(\rho_0 \bar{u}_i \bar{u}_j)] - c_p \Theta_o (ik_i \hat{\bar{\pi}}' + \frac{\partial \hat{\bar{\pi}}'}{\partial z}\delta_{i3})$$
$$+ \frac{g}{\Theta_o}\hat{\bar{\theta}}'\delta_{i3} + \mathcal{F}[\frac{1}{\rho_0}\frac{\partial}{\partial x_j}(\rho_0 \bar{\tau}_{ij})],$$

where $\mathcal{F}$ denotes the horizontal Fourier transform. Multiplying by $\frac{1}{2}\rho_0 \hat{\bar{u}}_i^*$ and adding the complex conjugate, the resulting equation is:

$$\frac{\partial E}{\partial t}(\vec{k}, z) = T(\vec{k}, z) + P(\vec{k}, z) + B(\vec{k}, z) + D(\vec{k}, z), \tag{3}$$

where

$$T(\vec{k}, z) = -\operatorname{Re}(\hat{\bar{u}}_i^* \mathcal{F}(\frac{\partial}{\partial x_j}(\rho_0 \bar{u}_i \bar{u}_j))),$$

$$P(\vec{k}, z) = c_p \Theta_0 \rho_0 \operatorname{Re}(-ik\hat{\bar{u}}^*\hat{\bar{\pi}}' - il\hat{\bar{v}}^*\hat{\bar{\pi}}' - \hat{\bar{w}}^*\frac{\partial \hat{\bar{\pi}}'}{\partial z}),$$

$$B(\vec{k}, z) = \frac{g}{\Theta_0}\operatorname{Re}(\rho_0 \hat{\bar{w}}^*\hat{\bar{\theta}}'),$$

$$D(\vec{k}, z) = \operatorname{Re}(\hat{\bar{u}}_i^* \mathcal{F}(\frac{\partial}{\partial x_j}(\rho_0 \bar{\tau}_{ij}))).$$

Run	(L,H) [m]	(n,m)	(dx,dz) [m]	Q_s [Kms^{-1}]
B40	(5750,1990)	(144,50)	(40.2,40.6)	0.071
B20	(5750,1990)	(288,100)	(20.0,20.1)	0.071
B10	(5750,1990)	(576,200)	(10.0,10.0)	0.071
B5	(5750,1990)	(1152,400)	(5.0,5.0)	0.071
H40	(5750,1990)	(144,50)	(40.2,40.6)	0.142
H20	(5750,1990)	(288,100)	(20.0,20.1)	0.142
H10	(5750,1990)	(576,200)	(10.0,10.0)	0.142
D80	(11500,1990)	(144,50)	(80.4,40.6)	0.071
D40	(11500,1990)	(288,100)	(40.7,20.1)	0.071
D20	(11500,1990)	(576,200)	(20.0,10.0)	0.071

Table 1.: Domain size, number of grid points, grid spacings, and surface heating strength for each numerical experiment.

The evolution of $E(\vec{k}, z)$ is defined by four terms: the advection or nonlinear transfer $T(\vec{k}, z)$, the pressure term $P(\vec{k}, z)$, the buoyancy flux or heat flux $B(\vec{k}, z)$, and the SGS dissipation $D(\vec{k}, z)$. The pressure term P can be rewritten using the continuity equation,

$$-ik(\rho_0\hat{\bar{u}}^*) - il(\rho_0\hat{\bar{v}}^*) + \frac{\partial}{\partial z}(\rho_0\hat{\bar{w}}^*) = 0,$$

as:

$$P(\vec{k}, z) = -c_p\Theta_0\,\mathrm{Re}\big(\frac{\partial}{\partial z}(\rho_0\hat{\bar{w}}^*\hat{\bar{\pi}}')\big), \tag{4}$$

which implies that it goes to zero when integrated over the depth of the domain. From these quantities, we can compute one-dimensional spectra in terms of the horizontal wavenumber $k_h = \sqrt{k^2 + l^2}$ by binning over k and l in the usual way [36]. In most of what follows spectral quantities are averaged over the depth of the domain although the z dependence is discussed for the heat flux, nonlinear transfer, and dissipation spectra.

In order to compute profile statistics and spectra, which requires all model fields on a common grid, we use spectral interpolation in the horizontal, i.e. FFT's of $\hat{\bar{u}}$ and $\hat{\bar{v}}$ are taken at the staggered points and then corrected by multiplication by $e^{-ik(\frac{\Delta x}{2})}$ and $e^{-il(\frac{\Delta y}{2})}$ respectively. Derivatives in the transfer, dissipation, and pressure spectra are computed from the unstaggered fields spectrally in the horizontal and using fourth order finite differences in the vertical. Thus each term in the budget is calculated at order of accuracy at or above what is used in the underlying numerical model. There are errors associated with the fact that we use interpolation and finite difference schemes in post-processing that differ from the underlying model. For example these errors prevent us from balancing the terms in the spectral budget to machine precision at each wavenumber. These errors remain relatively small however and do not affect the conclusions of this study which are focused on the larger scale features of the spectral budget.
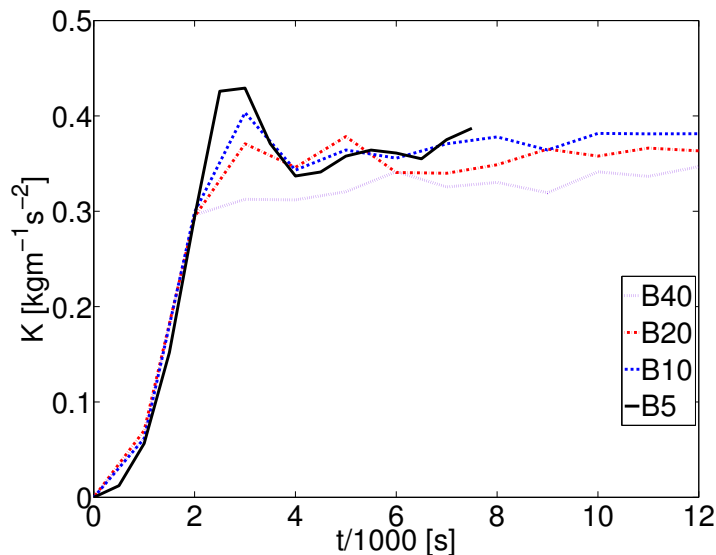
Figure 2.: Time series of volume mean kinetic energy for experiments B40-B5.

3.   Results

3.1.   *Overview of Simulations*

Because our primary focus is on the kinetic energy spectral budget for the CBL at equilibrium, we run each simulation up to statistical stationarity as determined from time series of the volume mean kinetic energy:

$$K = \frac{1}{d} \int_0^d \frac{1}{2} \rho_0 \langle (\bar{u}^2 + \bar{v}^2 + \bar{w}^2) \rangle \, \mathrm{d}z,$$

where $\langle \rangle$ denotes horizontal average. The time series for experiments B40-B5 are show in Figure 2. The flow has reached approximate stationarity by 4000 s. Vertical profiles of horizontally averaged potential temperature and heat flux are plotted in Figure 3(a,b). The results show nearly identical potential temperature profiles, which implies that the equilibrium potential temperature structure is independent of resolution. The heat flux profiles differ between resolutions only in the entrainment layer and the surface layer, where increased resolution causes sharper adjustment between adjacent layers. Velocity variance profiles are shown in Figure 3(c,d): the vertical velocity variance is largest within the mixing layer, while the horizontal variance has peaks within the entrainment zone and the surface layer. Interestingly, the horizontal variance shows significant dependence on resolution, not just in the entrainment and surface layers, but also within the mixing layer, but the profiles appear to be converging with increasing resolution. A discrepancy exists in the plots of vertical and horizontal velocity variances where for increasing resolution (runs B40, B20, & B10) the variances increase slightly while for the highest resolution (run B5) there is an unexpected decrease. This may be caused by the fact that the highest resolution was only averaged up to 7500 s instead of the full 12000 s. However, other studies [14, 41] have also shown significant scatter rather than a monotonic increase in the mixing layer velocity variances as resolution is increased.

    Overall, a high degree of convergence is seen in all the plots and the shapes of these statistics are consistent with previous studies of dry convective boundary
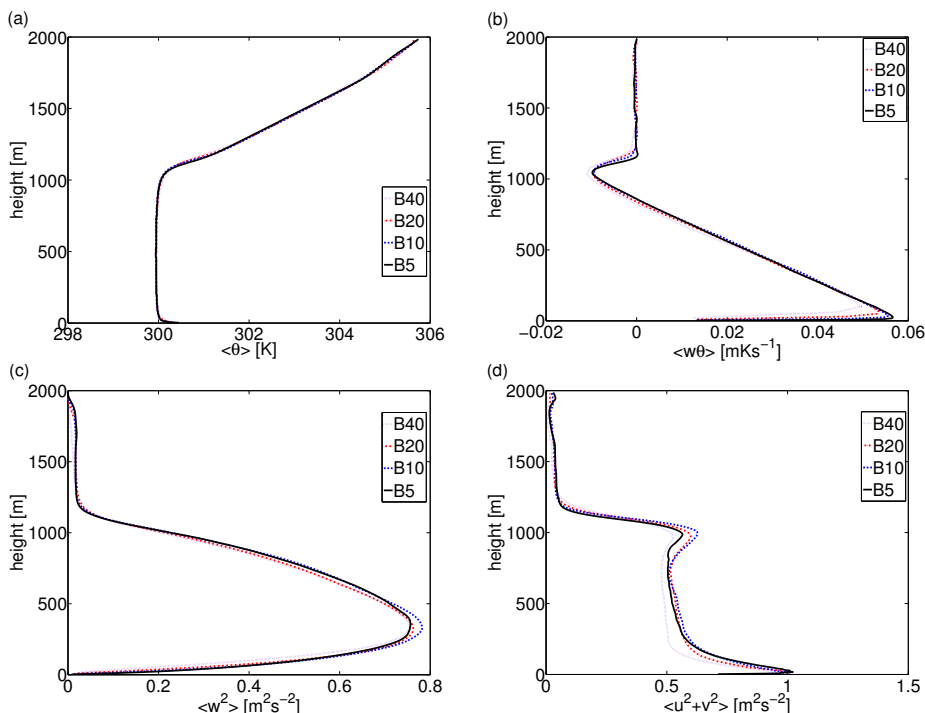
Figure 3.: Horizontally and time averaged (a) potential temperature, (b) heat flux, (c) vertical velocity variance, and (d) horizontal velocity variance for experiments B40-B5.
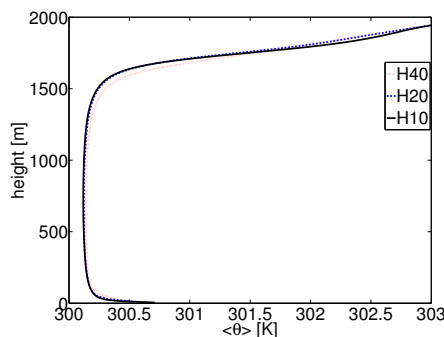

Figure 4.: Horizontally averaged potential temperature for experiments H40-H10.

layers [14, 25, 26, 41]. Statistics for the larger domain size and larger surface heat flux experiments have similar profiles are not shown. Potential temperature profiles from the simulations with higher surface heat flux are shown in Figure 4. The effect of increased Q_s on the boundary layer thickness from approximately 1100 m and 1600 m is clearly visible.

Figure 5 shows vertical slices of the model fields at the final time of the highest resolution run B5. The corresponding heat flux is shown in Figure 6. By this time the boundary layer height has reached its equilibrium level and a balance has been achieved between the surface heating, radiative cooling, and subsidence. Several rising plumes can be seen with positive potential temperature perturbations. Additionally, plume cores exhibit strong positive vertical velocity and positive heat flux. Outside these plume cores, but still within the plume structure, there exist regions of positive temperature perturbations and negative vertical velocity corresponding to negative vertical heat flux. These regions of negative heat flux are likely the result of the highly turbulent mixing that the plumes generate, particularly on their outer shell. Often the plumes may extend the entire boundary layer
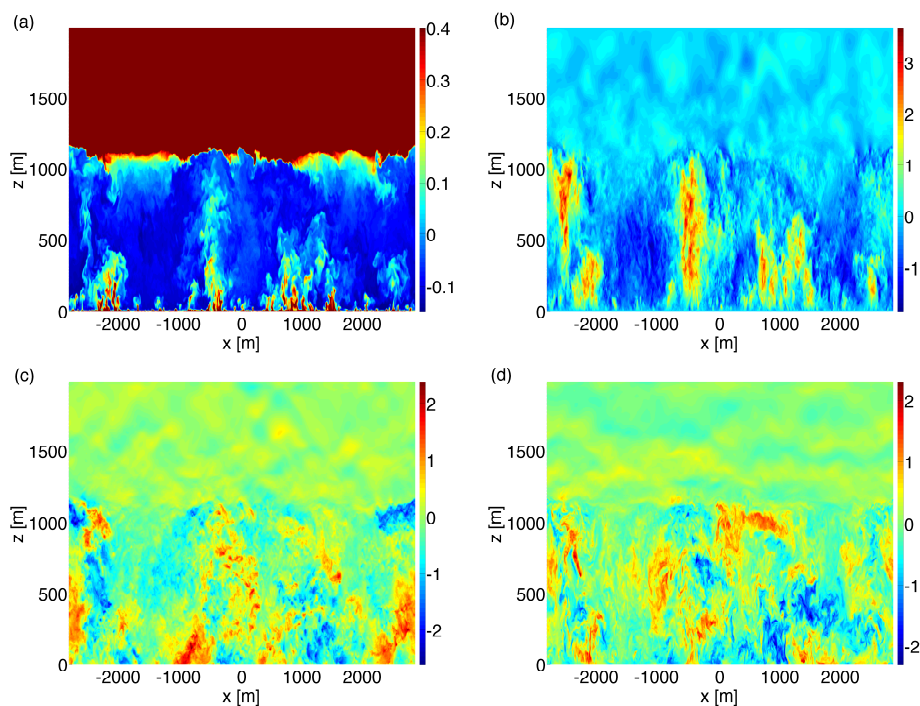
Figure 5.: Vertical (x-z) slices of (a) θ', (b) w, (c) u, and (d) v taken at $y = 0$ m and time 12000 s for experiment B5.

depth and may even penetrate into the stable layer resulting in sharp potential temperature changes at the plume/stable layer interface [2]. To the side of these penetrating plumes near the boundary layer height, warm air is often seen being pulled downward into the mixing layer as is most clearly seen in an animation of the potential temperature perturbation [2]. Well within the mixing layer, the plumes themselves are separated by large regions of sinking air (Figure 6). Generally within the mixing layer these regions correspond to cooler sinking air (positive vertical heat flux), but as we approach the entrainment layer there exists regions of hotter sinking air (negative vertical heat flux). Finally both horizontal velocities (u and v) exhibit equally sized regions of positive and negative velocities. No significant difference is observed between the u and v velocities which is consistent with the lack of background shear.

3.2.   *Spectral Kinetic Energy Budget*

3.2.1.   *Heat Flux*

Of the various terms in the spectral KE budget, we consider first the heat flux $B(k, z)$, which plays a key role as the source of KE in the CBL. We have shown above that the averaged physical space statistics, i.e. the velocity variances and heat flux, match what has been seen in numerous other LES studies. In particular the physical space heat flux profile appears to have almost completely converged for run B5 which might mean that run B5 is sufficiently resolved. However, an important question is whether the spectral quantities exhibit similar convergence. Indeed, if the heat flux spectrum has a broad and resolution-dependent contribution from intermediate and small scales, this could have implications for the development of a locally isotropic inertial range.

Heat flux spectra from run B5 at different vertical levels are shown in Figure 7 (spectra are labeled with wavelength $\lambda = 2\pi/k$ along the x axis for clarity). As
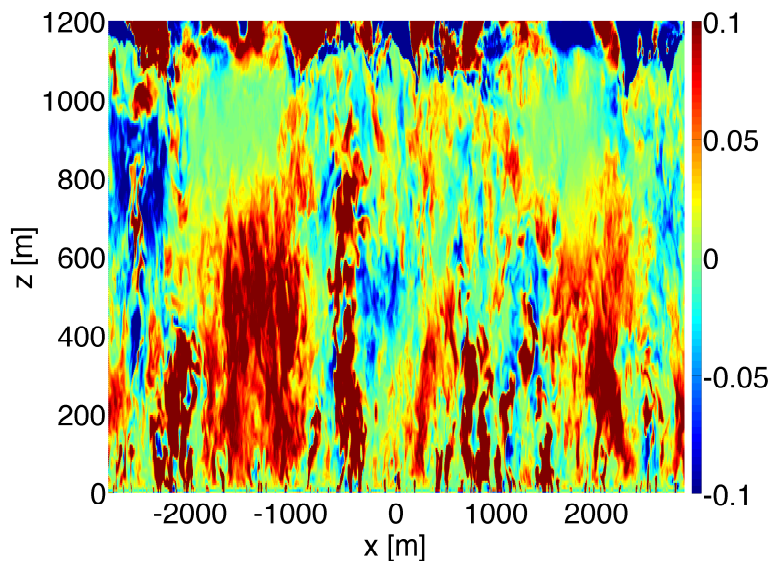
Figure 6.: Vertical heat flux, $w\theta'$, taken at $x - z$ slice $y = 0$ m and time 12000 s for run B5

expected the heat flux near the surface is positive and peaked at large wavenumber implying a small scale injection of KE [1–3]. Moving up through the mixing layer the spectrum remains positive but the peak shifts to larger scales [1–3]. This transition of the maximum heat flux from smaller scales to larger scales as one moves up through the mixing layer is consistent with horizontal slices of potential temperature and heat flux (Figure 8). Near the surface, heating causes the formation of fine filamentary structures reminiscent of the honeycomb patterns seen in Rayleigh-Bernard flows. Well within the mixing layer, however, large-scale thermal plumes have formed with diameters around 100-500 m which are associated with the larger scale heat flux. At higher levels near the entrainment zone strong negative values of the heat flux are obtained at large scales corresponding to the downward movement of warmer stably stratified air being pulled into the mixing layer.

The peaks of positive flux transition from small scales in the surface layer to large scales in the mixing layer. This transition occurs rapidly with increasing height, suggesting that the surface layer occupies only the bottom $O(10)$ m and that the large-scale thermal plumes begin forming at height relatively close to the surface. This surface layer however is likely not resolved by the Smagorinsky parameterization and its detailed structure requires further fine resolution experiments beyond the scope of the current study. Within the mixing layer, the location of the peak positive flux was found to remain approximately constant around $\lambda \sim 1150$ m for all the base case experiments (B40-B5) and the larger domain sized experiments (D80-D20). There is, however, a shift in the peaks to larger scales for the case of stronger surface heating (runs H40, H20, and H10). This is not surprising as the peak follows the scale of the boundary layer depth and the higher surface heating experiments naturally result in deeper boundary layers. Once the boundary layer height is reached, the peaks in positive flux move to small scales again where they do not inject a significant amount of energy in the entrainment layer.

While the large scale injection of kinetic energy by positive heat flux appears to remain approximately independent of resolution and domain size and only moves to large scales for the higher surface heating, the contribution from small scales is more sensitive; such small-scale forcing could have implications for the existence
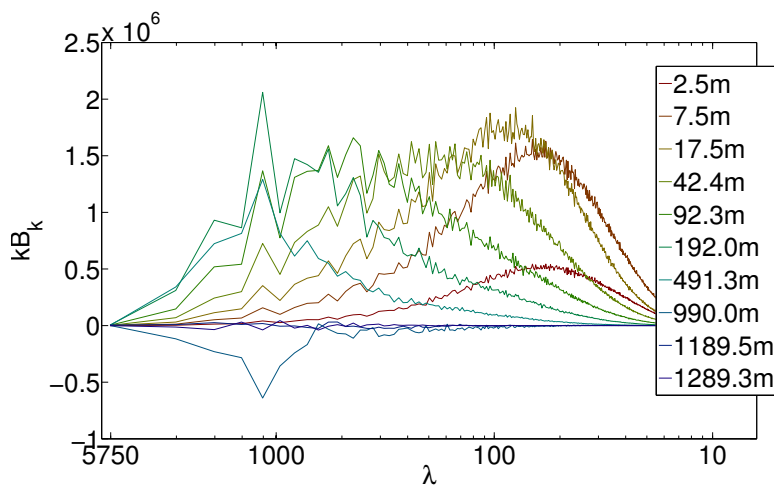
Figure 7.: Time averaged horizontal heat flux spectra at different height levels for run B5. Spectra have been multiplied by k_h to preserve area on the log-linear plot.
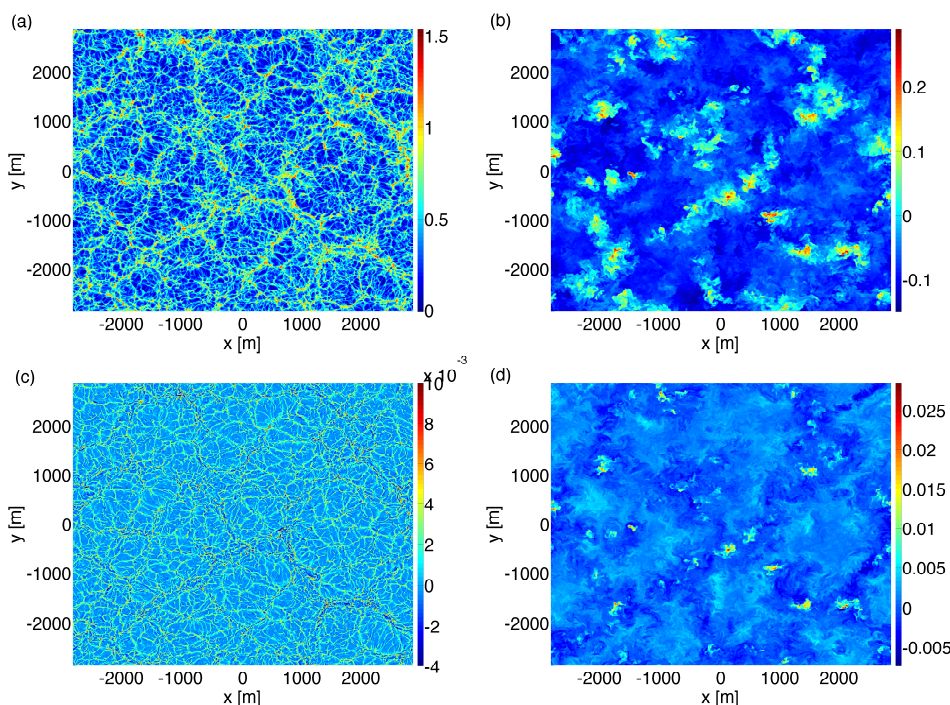

Figure 8.: Horizontal (x-y) slices of $\bar{\theta}'$ at (a) $z = 2.5$ m, (b) $z = 501$ m, and of $\frac{g}{\Theta_0}\bar{w}\bar{\theta}'$ at (c) $z = 2.5$ m, (d) $z = 501$ m.

of an inertial range removed from the forcing, since it could signify injection of KE over a broad range of scales, possibly down to the LES dissipation scale. In order to compare the heat spectra of different resolutions, we plot them together in Figure 9 averaged over the depth of the domain. These spectra are consistently broadening as resolution increases. This broadening also holds for the larger domain experiments as well as the larger surface heating experiments. On the other hand, the large scale contributions appear to remain relatively independent of resolution. These heat flux spectra do appear to exhibit a saw-tooth pattern in the large scales. This seems to be an artifact of the binning over annuli on the k_x-k_y plane, time sampling, and the fact that heat flux spectra, which are not positive definite, are generally much more noisy than kinetic energy spectra (e.g. see [42]).
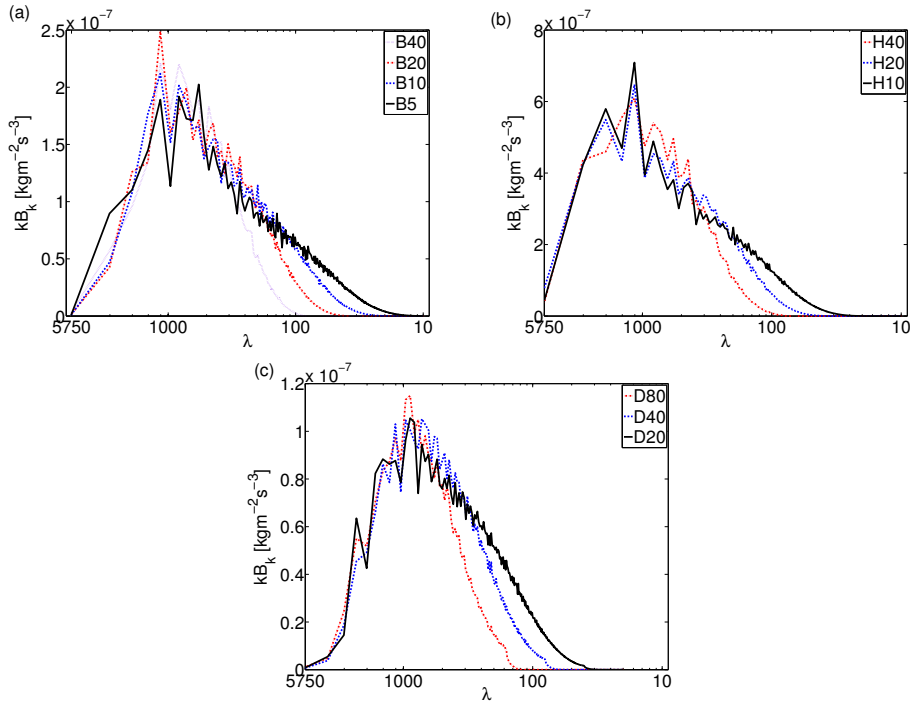
Figure 9.: Time averaged heat flux spectra averaged over the boundary layer depth for (a) the base runs B40-B5, (b) the enhanced surface heat flux runs H40-H10, and (c) the large domain runs D80-D20. Spectra have been multiplied by k_h to preserve area on the log-linear plot.
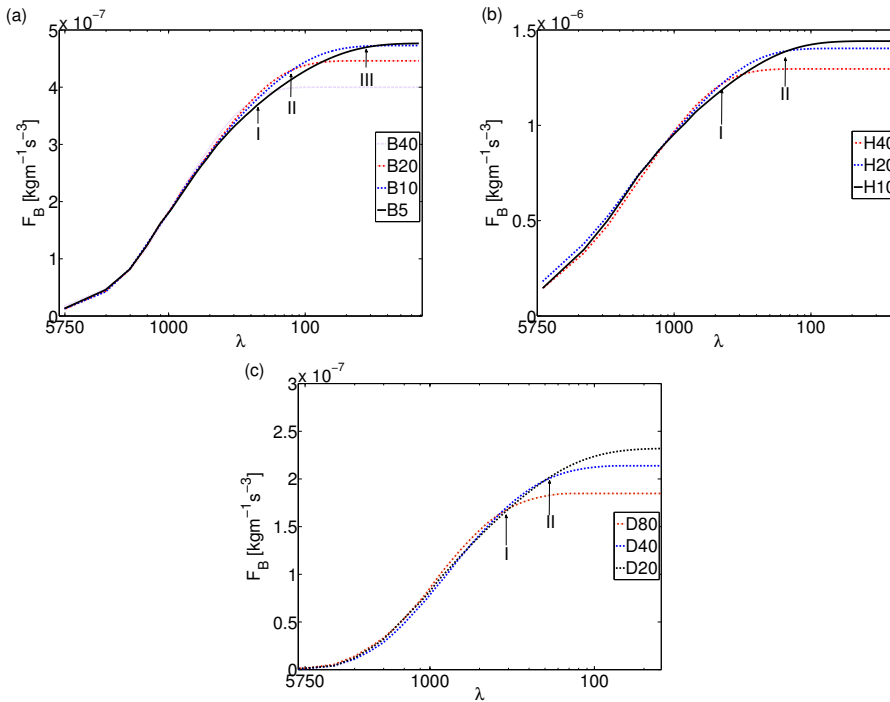

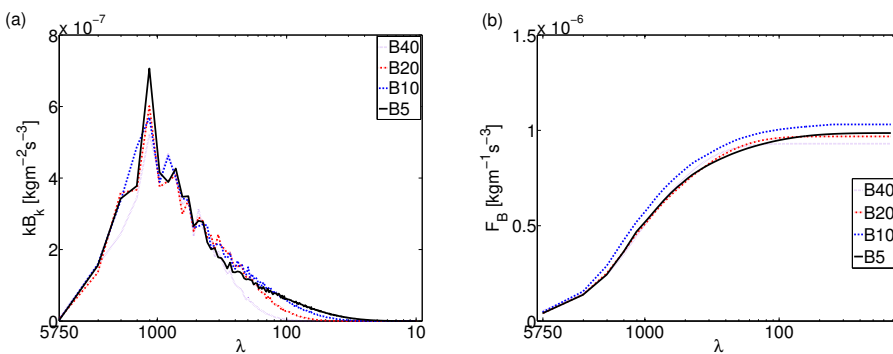Figure 10.: Integrated heat flux $F_B(k)$ for all runs. Other details are as in Figure 9.

Figure 11.: (a) Time-averaged heat flux spectra averaged throughout mixing layer ($z = 200 - 800$ m) for runs B40-B5. Spectra have been multiplied by k_h to preserve area on the log-linear plot. (b) $F_B(k)$ within mixing layer for runs B40-B5.

We also compute the integral of the heat flux spectra as a function of wavenumber:

$$F_B(k) = \int_0^k B_k(k')dk', \tag{5}$$

which gives the contribution to the total injection rate of KE from heat flux from wavenumbers less than k. The integral of the vertically averaged heat flux spectra is shown in Figure 10. As the resolution increases, $F_B(k)$ is seen to converge at small scales. Consider the B runs in Figure 10(a): the wavenumber below which $F_B(k)$ has converged with resolution (marked out by I, II, & III) moves further to the right as resolution increases. For example, as Δx is decreased from 20 m to 10 m, there is a 6% increase in the total wavenumber-integrated heat flux. Figures 9 and 10 indicate that the heat flux spectrum, while peaked at large scales, has a positive contribution over a broad range of scales; fine grid spacings of $\Delta x \sim 5$ m are required for the total wavenumber-integrated heat flux to converge.

It is possible that the small-scale heat flux contribution is caused solely by the surface layer where small scale convective motions are most likely to occur, given that most of the contribution to the heat flux spectrum in the surface layer is at small scales (see Figure 7). To investigate this, we plot the heat flux spectra averaged over the mixing layer ($z = 200 - 800$ m; see Figure 11) and surface layer ($z = 0 - 100$ m; see Figure 12). It is clear that a rightward shift in B_k to smaller scales with increased resolution exists for both regions; however, the shift is significantly smaller for the mixing layer than for the surface layer. Near the surface a combination of diffusion and small scale convective motions transports the surface heat into the overlying air. Thus by increasing resolution, we are resolving these features more and hence capturing them in the surface layer heat flux spectra. By contrast, the mixing layer heat flux is dominated by larger structures and is more robust to changes in resolution.

3.2.2.   *Transfer, Dissipation, & Pressure*

The remaining terms in the spectral kinetic energy budget for the base case experiments are plotted in Figure 13, while the budgets for the highest resolution experiments B5, H10, and D20 are shown in Figure 14. The transfer, pressure, and dissipation spectra are all plotted on the same axis (along with the heat flux spectra discussed in section 3.2.1) in order to highlight the relative strength, and related large and small scale features, of each term within a statistically stationary CBL. Each term in the budget extends to a maximum horizontal wavenumber of
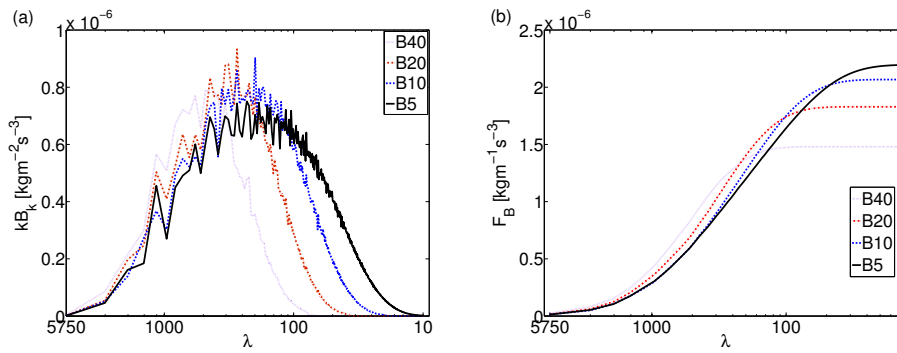
Figure 12.: (a) Time-averaged heat flux spectra averaged throughout surface layer ($z = 0 - 100$ m) for runs B40-B5. Spectra have been multiplied by k_h to preserve area on the log-linear plot. (b) $F_B(k)$ within surface layer for runs B40-B5.
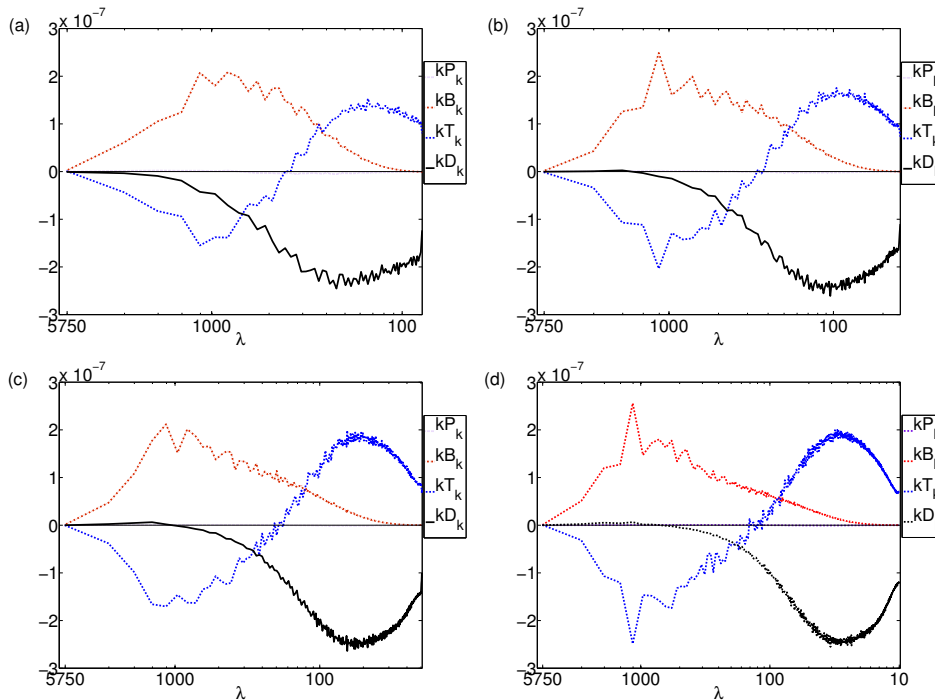

Figure 13.: Time averaged terms in the spectral budget, averaged in z over the boundary layer depth, for runs (a) B40, (b) B20, (c) B10, and (d) B5.

$k_{max} = \pi/\Delta x$, and so with each successive increase in resolution the spectra are extended to smaller scales.

The role of each term in the budget is evident from the evolution equation of the kinetic energy spectrum (3). When the time rate of change of the spectral kinetic energy is zero (as is approximately the case for time-averaged spectra in a statistically stationary boundary layer), the heat flux (B_k), transfer (T_k), pressure (P_k), and dissipation (D_k) spectra must balance. In each plot we see that energy is injected over a rather broad range of scales, but most significantly at larger scales, by the heat flux spectra as was previously discussed. Energy is then removed from the relatively large scale region (negative transfer spectra), and injected into the small scales (positive transfer spectra). Once transferred, the energy at small scales is dissipated by the LES model through the eddy viscosity parameterization of the SGS fluxes at large wavenumbers (negative dissipation spectra), as expected for a downscale energy cascade.

We have also included plots showing the transfer and dissipation spectra at
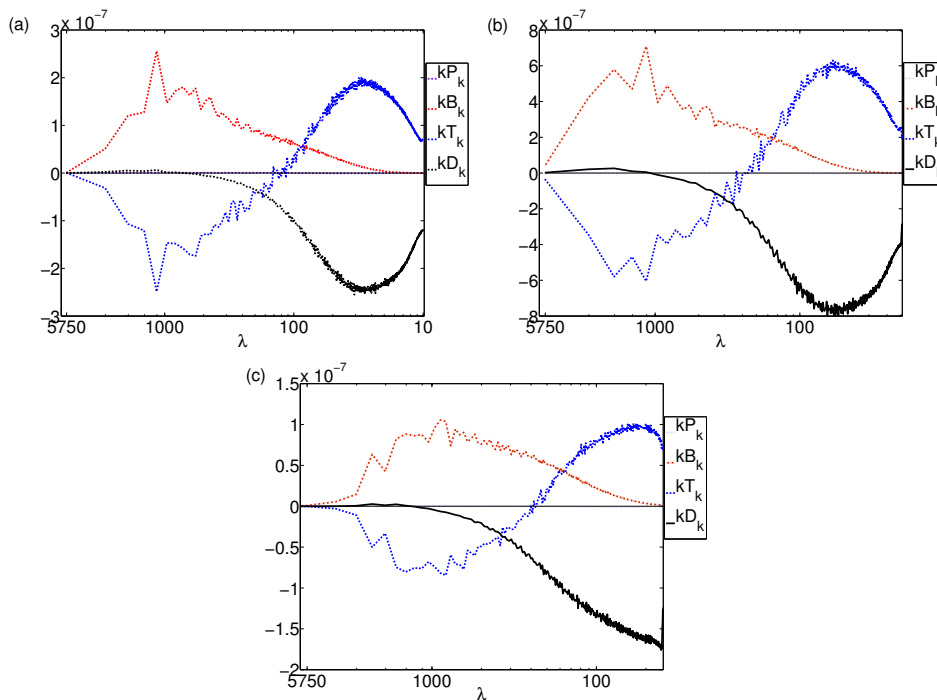
Figure 14.: Time averaged terms in the spectral KE budget, averaged in z over the boundary layer depth, for runs (a) B5, (b) H10, and (c) D20.
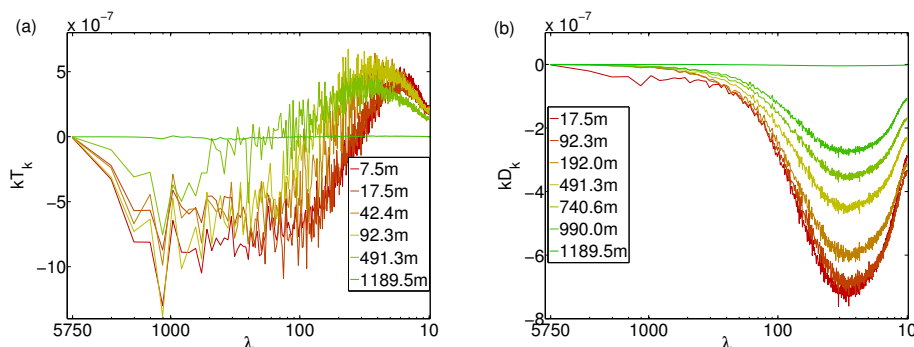

Figure 15.: (a) Time averaged horizontal transfer spectra at different levels for run B5. (b) Time averaged horizontal dissipation spectra at different levels for run B5. Spectra have been multiplied by k_h to preserve area on the log-linear plot.

different heights (Figure 15). The transfer generally shows a cascade from large scales to small scales consistent with the domain averaged spectra. The dissipation spectra also shows a similar profile to the domain averaged plots, except that we can see that this spectra is strongest within the first 500 m where the thermal plumes are developing. As we move through the mixing layer the strength of the dissipation decreases until we reach the boundary layer height at which point the dissipation turns off. This is consistent with the fact that the eddy viscosity becomes zero within the stable layer for the Smagorinsky model.

The vertically integrated pressure spectrum is approximately zero in all cases, as expected since $w = 0$ at the upper and lower boundaries (4). The small deviations from 0 arise as a result of the interpolation of variables to the thermal points which results in small errors. We have confirmed that these small errors decrease as resolution is increased. The pressure perturbation spectra at a given horizontal slice is not zero, and in fact may be rather large near the surface where strong surface heating and large vertical w velocity gradients exist (not shown).
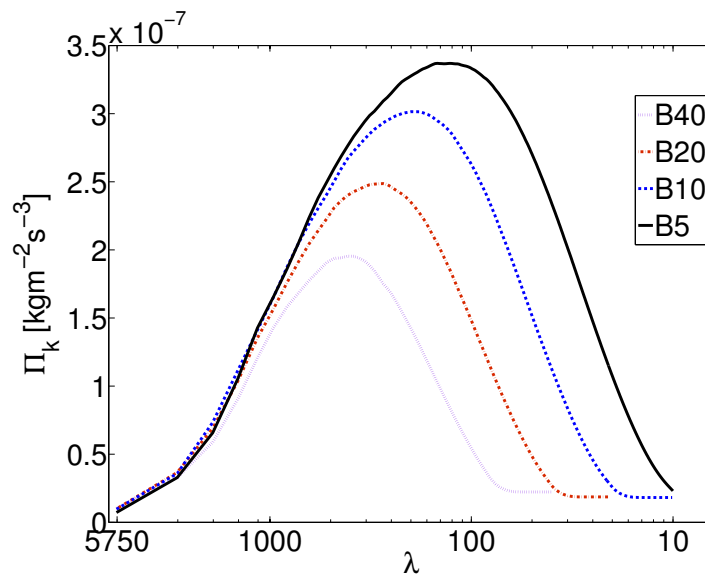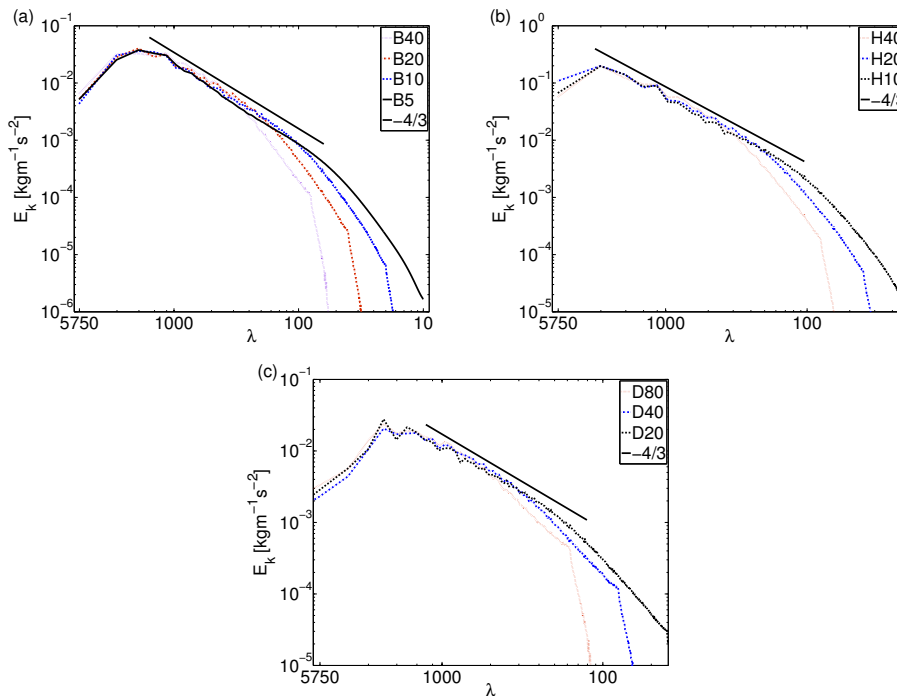
Figure 16.: Spectral flux for experiments B40-B5.

Figure 17.: Time averaged KE spectra, averaged in z over the depth of the boundary layer, for (a) the base runs, (b) the enhanced surface heat flux runs, and (c) the larger domain runs, all at different resolutions.

In all cases, the large-scale transfer spectra and heat flux spectra are in balance, consistent with the statistical stationarity of the averaging interval. The higher surface heat flux experiments (Figure 14 b) have large-scale heat flux and transfer spectra with magnitudes approximately twice that of their lower surface heat flux counterparts, in line with the stronger forcing of these runs. In the case of the larger domain (Figure 14 c) the wavenumber axis extends further to the left (larger-scales); however the heat flux and transfer spectra remain approximately unchanged from the smaller domain case, implying that the budget is insensitive to domain size. Thus increasing the domain size does not result in the organization

Run	m	a	λ range
B40	-1.4549	-10.9464	$1150 < \lambda < 302.6$
B20	-1.3503	-10.6660	$1150 < \lambda < 198.3$
B10	-1.3410	-10.6494	$1150 < \lambda < 130.7$
B5	-1.4088	-11.0234	$1150 < \lambda < 83.3$
H40	-1.5837	-10.5009	$1150 < \lambda < 302.6$
H20	-1.4150	-9.9946	$1150 < \lambda < 198.3$
H10	-1.3697	-9.8427	$1150 < \lambda < 130.7$
D80	-1.3222	-10.6365	$1150 < \lambda < 575$
D40	-1.2931	-10.4577	$1150 < \lambda < 338.2$
D20	-1.2678	-10.8854	$1150 < \lambda < 250$
BTKE40	-1.3740	-10.9435	$1150 < \lambda < 302.6$
BTKE20	-1.3657	-10.9097	$1150 < \lambda < 198.3$

Table 2.: Values of a and m computed by least squares assuming KE spectra have the form $y = e^a k_h^m$.

of larger-scale features within the flow in a significant way as might be expected in simulations with strong background rotation (e.g. [37]) or as has been seen in temperature spectra (e.g. [42]) and experiments involving moisture (e.g. [43]).

The spectral budget at small scales is dominated by the dissipation; however, it is significant that in all experiments there is broad overlap between the heat flux and dissipation spectra. This overlap follows from the fact that, as discussed above, the heat flux spectrum is very broad and extends to smaller scales as resolution is increased. Only in the highest resolution case (Figure 13 d) do we begin to reduce this overlap. As a result none of the experiments show a resolved inertial range of intermediate wavenumbers with approximately zero transfer. For more insight into the existence (or not) of an inertial range in these simulations, we compute the spectral flux:

$$\Pi_k = -\int_0^k T_k(k')dk'.$$

An inertial range corresponds to a range of k with constant spectral flux, and is a fundamental assumption in the derivation of the Kolmogorov -5/3 spectrum [38]. The spectral flux for experiments B40-B5 are shown in Figure 16. No inertial range emerges as resolution is increased; instead, the maximum spectral flux increases and shifts to smaller scales. This increase and shift is perhaps caused by the small-scale heat flux that develops as resolution increases and by the fact that increased resolution results in the dissipation spectra also moving to smaller and smaller scales. Thus the transfer spectra must make up the difference in the budget.

The kinetic energy spectra for each experiment are shown in Figure 17. Assuming KE spectra of the form:

$$y = e^a k_h^m,$$

we can use least squares to find a and m for regions where the spectra have approximately constant slope in the log-log plots (Table 2). All the experiments have KE spectra with slopes slightly shallower than $-5/3$. For the base case experiments and the higher surface heating experiments the KE slopes appear to be closer to $-4/3$. For the larger domain experiments the slopes appear to be slightly shallower
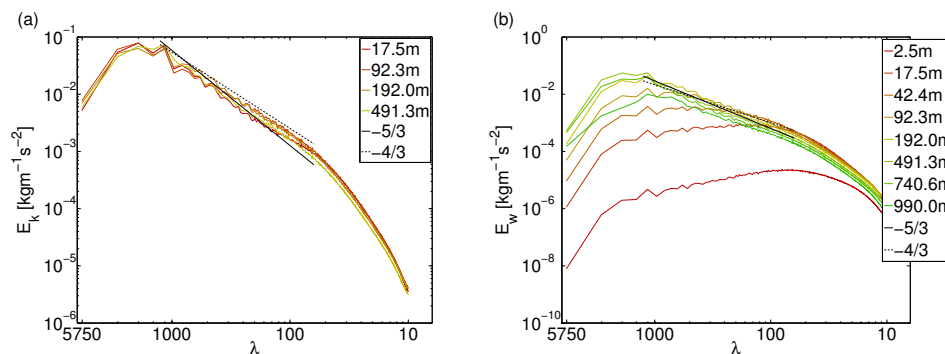
Figure 18.: (a) Time averaged KE spectra at different levels for run B5. (b) Time averaged spectra of vertical KE at different levels for run B5.
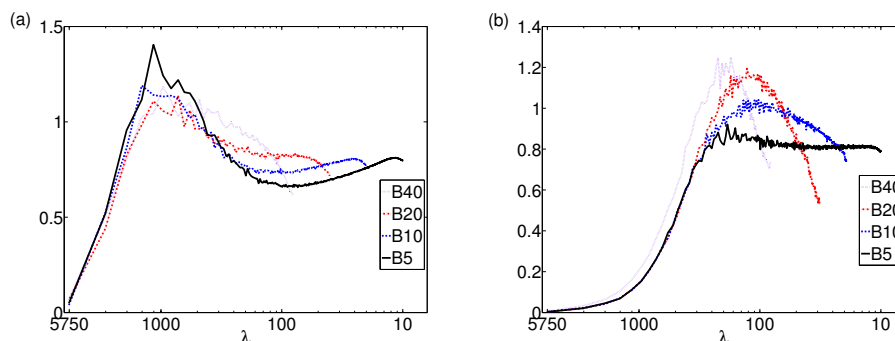

Figure 19.: a) Ratio of vertical to horizontal kinetic energy spectra averaged in the vertical over whole domain, b) vertical-to-horizontal ratio of energy spectra averaged in the surface layer ($z = 0 - 100$ m)

then $-4/3$. For the experiments with higher surface heat flux, the spectra have a larger magnitude, in line with the stronger surface forcing. In all cases, the spectra peak at wavenumbers related to the boundary layer depth. In the SGS dissipation range at large k_h, the spectra become shallower as resolution is increased which indicates that the model becomes less dissipative as resolution is increased. In the previous section we saw that the heat flux spectrum injects significant energy over a wide range of scales throughout all the CBL layers. It is possible that this broad-scale forcing is responsible for these spectra being consistently shallower than the theoretical $-5/3$ power law. Surface layer effects may also be important here. In Figure 18 we show the KE spectra and the spectrum of vertical KE at different levels. For example, in computing the spectrum of vertical kinetic energy within the mixing layer we found that the slope more closely resembled a $-5/3$ scaling, consistent with [14], while the full KE spectra remain closer to $-4/3$.

The energy spectra in Figure 17 are clearly shallower than what we would expect for isotropic 3D turbulence. To investigate this discrepancy further, we consider whether local isotropy is emerging at small scales in the highest resolution cases. In isotropic turbulence, the ratio of one-dimensional transverse and longitudinal energy spectra (e.g. k_x spectra of KE in w and u) will attain a constant value near $4/3$ when local isotropy is reached [15]. Because we compute two-dimensional horizontal wavenumber spectra however, a modification of the $4/3$ isotropy condition is required. Defining the horizontal wavenumber spectra of horizontal and vertical KE over cylindrical wavenumber shells results in an isotropic vertical-to-horizontal ratio of approximately 0.57 (see Appendix). Of course, this theoretical ratio assumes a $-5/3$ spectrum; isotropic turbulence with a $-4/3$ ratio would likely have a slightly smaller ratio. We plot this ratio for experiments B40-B5 in Figure 19

(a). At large scales this ratio is larger than 1 and progressively moves lower as we transition to small scales indicating that within the large-scales the vertical motions are more energetic than the horizontal. In fact, increased resolution results in higher ratios at large-scales, suggesting that lower resolution simulations suppress the relative strength of the vertical KE. While the low resolution experiment B40 takes on a ratio that is roughly a constant value near 1 over all wavenumbers (although it does decrease below 1 as we move to smaller scales), the higher resolution experiments seem to form plateaus at successively smaller values below 1 as resolution is increased. For the highest resolution experiment this ratio is approximately equal to $0.65 - 0.70$ for λ in the range $30 - 160$ m. Thus with increasing resolution, the ratio might be approaching 0.57 from above. The finding that this ratio is generally larger than the theoretical value for isotropic turbulence agrees with previous results [2, 13, 16]. Finding spectral ratios of 0.57 is only a necessary condition of local isotropy, however these results suggest that local isotropy, if it emerges, would require grid spacings $< O(1)$ m.

In order to further investigate the effect of the surface heating on the energy spectra, we compare the spectral ratios restricted within the surface layer ($z = 0 - 100$ m). These results are shown in Figure 19 (b). Unlike in the domain-averaged case, the vertical-to-horizontal ratio does not show peaks in the large-scales indicating that the vertical energy spectra is much weaker than the horizontal energy spectra at these scales. This confirms that within the surface layer the vertical spectra remain energetic primarily in the small-scales and this property can also be seen in Figure 18. We have confirmed however that the horizontal spectra do peak at large scales. Thus within the surface layer the horizontal and vertical energy spectra differ significantly in the large-scales. Even for the highest resolution case, the ratio of vertical to horizontal KE is around 0.8, suggesting that the surface layer turbulence remains much more anisotropic than the mixed layer.

3.2.3. *Sensitivity to SGS Parameterization*

We have seen that the dissipation spectrum is shifted to small-scales as resolution is increased. An important question then is what effect do alternative subgrid-scale parameterizations have on the spectral KE budget; in particular do more sophisticated parameterizations result in less dissipation in the large scales and a greater shift in the peak dissipation to small scales for a given resolution? Previous studies (e.g. [22, 25]) have found that both physical space statistics and energy spectra were relatively robust to changes in the SGS parameterization. To investigate the SGS sensitivity of the current study, we re-run some of our experiments using the TKE model [9]. We solve the same equations as before (1), except that now the eddy-viscosity is changed to:

$$K_m = 0.1 l_m \sqrt{e}, \quad K_h = (1 + \frac{2l_m}{l_n}) K_m,$$

where e is the turbulent kinetic energy and is found by solving an additional prognostic equation [9]. The subgrid-scale mixing length l_m, and the grid-scale l_n, are defined as:

$$l_m = \min{(0.82\sqrt{\frac{e}{max(\epsilon, N^2)}}, l_n)} \quad l_n = \sqrt{\frac{1}{(\frac{1}{\Delta x})^2 + (\frac{0.23}{z\kappa})^2}},$$

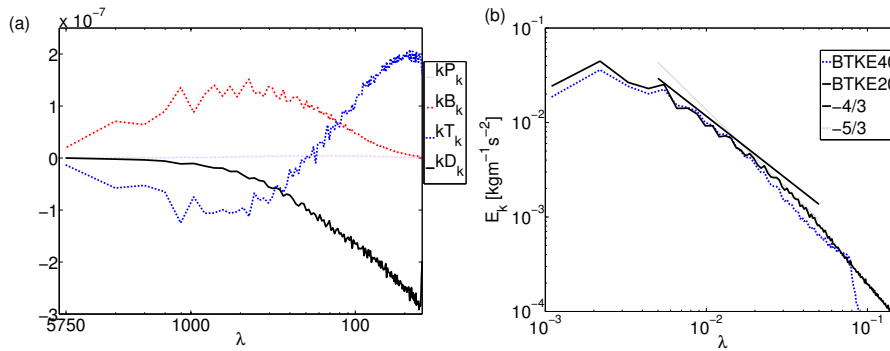where $\epsilon = 10^{-12}$. Thus K_h/K_m ranges between 1 and 3 and the SGS mixing length

Figure 20.: a) Spectral KE budget for BTKE20. b) KE spectra for BTKE40 and BTKE20.

l_m is at most l_n, but can be much smaller in stably stratified regions. We run this model only for the experiments B40 and B20 and refer to the TKE runs as BTKE40 and BTKE20. The resulting spectral budget and KE spectra are shown in Figure 20(a,b).

A number of important conclusions can be derived from these results. Firstly, the dissipation spectrum is seen to peak at smaller scales with the TKE model than it did with the Smagorinsky model for a fixed resolution. In fact for the experiment BTKE20, the dissipation spectrum peaks at wavenumber close to where the highest resolution (B5) Smagorinsky dissipation spectrum peaked despite being a quarter of the resolution. Nevertheless, even for the TKE runs the heat flux spectrum remains quite broad and the transfer spectra still does not show any region of constant spectral flux (not shown). The decreased dissipation does however have an effect on the KE spectra by decreasing the slope within the SGS dissipation range. The approximately $-4/3$ slope for the KE spectra observed in the Smagorinsky model appears to remain unchanged when the TKE model is used indicating that this result is robust to changes in the SGS parameterization.

4.   Summary

In this paper we have presented large-eddy simulations of the dry convective boundary layer. The physical space statistics of the simulations are in good agreement with other recent high-resolution CBL studies [14, 24, 39]. The main contribution of this work is the calculation and analysis of the full spectral kinetic energy budget, which provides insight into the shape of the horizontal wavenumber KE spectrum. KE is injected via heat flux, the spectrum of which is peaked at large horizontal scales when integrated over the depth of the boundary layer. At large scales, the heat flux spectrum is balanced by the nonlinear transfer, which transfers energy to small scales where it is removed by the SGS dissipation. Increasing the surface heat flux leads to a larger injection of KE and therefore a stronger cascade to small scales. The domain size of 6 km seems sufficiently large to capture this cascade; the budget terms are robust to increases in the domain size.

While the convective boundary layer setup does not conform to a traditional triply periodic isotropic turbulence simulation, boundary-layer and atmospheric turbulence researchers have attempted to explain some of the characteristics of CBL flows using classical turbulence theories [2, 13, 16]. At first glance, the spectral budget seems to agree with this classic picture of three-dimensional turbulence with large-scale forcing and small-scale dissipation. However, this interpretation is complicated somewhat by the fact that the heat flux spectrum, which plays the

role of the KE forcing, is quite broad. Indeed, while the heat flux is peaked at scales of around 1 km, there is a significant injection of kinetic energy from smaller scales that emerges as the resolution increases. This small-scale heat flux is dominated by small eddies in the surface layer. Indeed, the integrated heat flux spectrum – i.e. the total injection rate of KE – only begins to converges with very fine grid spacings of $\Delta x = 5$ m. As a result, there is a significant degree of overlap of the heat flux and dissipation spectra, even in the highest-resolution experiments. This overlap raises doubts about the possibility of an inertial range in these simulations. Our suspicions here were confirmed by analysis of the spectral flux. Rather than a wavenumber range of constant spectral flux, which is expected for isotropic three-dimensional turbulence, we find that the flux is peaked at increasingly small scales as the resolution increases.

The kinetic energy spectra are consistently slightly shallower than what would be expected for isotropic three-dimensional turbulence, with spectral slopes closer to -4/3 rather than -5/3. This discrepancy with the classical theory is not surprising given the overlap between the forcing and dissipation spectra. It seems that the broad heat flux spectrum is injecting energy directly at intermediate and small scales, yielding a shallower energy spectrum than would otherwise be expected with purely large-scale forcing. Local isotropy was investigated by considering the ratio of the vertical and horizontal two-dimensional kinetic energy spectra, which gives a necessary condition for local isotropy. This ratio is larger than the theoretical value of 0.57 for isotropic turbulence, but seems to be approaching 0.57 at the smallest scales in the highest-resolution case. As a result, grid spacings of $\Delta x = 5$ m seem to be almost sufficient to result in ratios that match the theoretical value. This provides some evidence that higher resolution experiments might result in regions of local small-scale isotropy around scales of 5 m or less.

Overall, using the TKE parameterization resulted in dissipation spectra more restricted to small scales, i.e. peak was shifted further to small scales compared to the Smagorinsky model for a fixed resolution. The heat flux spectra however continued to inject energy at a broad range of wavenumbers and the transfer spectra did not show any range of constant spectral flux. Both of these results are consistent with the Smagorinsky model results. It is difficult to say whether the TKE model was more computationally efficient in terms of moving the dissipation spectra to small scales as compared with the Smagorinsky model since the TKE model required an additional equation for e to be integrated and thus naturally took longer to run. Precise timing results are not available because dedicated nodes were not used.

Despite the simple set-up, there remain a number of avenues for future work on this problem. First, it would be interesting to see whether higher resolution would yield an inertial range and a -5/3 spectrum at very small scales. Second, this work employs the Smagorinsky-Lilly SGS model (and some preliminary work with the TKE model), which is quite dissipative. Another choice of model, such as the dynamic Smagorinsky model [40], [25], might yield a wider range of undamped scales. Finally, it would be important to explore the effects of moisture on the spectral KE budget; latent heating may yield a heat flux spectrum more strongly peaked at small scales, with greater overlap with the dissipation spectrum. The budget diagnostics presented here could easily be adapted for the moist problem.

Acknowledgement(s)

and Engineering Research Council of Canada.

References

[1] J.C.Kaimal, J.C.Wyngaard, D.A.Haugen, O.R.Cote, Y.Izumi, S.J.Caughey, and C.J.Readings. *Turbulence structure in the convective boundary layer*, J. Atmos. Sci. 33 (1976), pp. 2152-2169.

[2] H.Schmidt and U.Schumann. *Coherent structure of the convective boundary layer derived from large-eddy simulations*, J. Fluid Mech. 200 (1989), pp. 511-562.

[3] R.Kaiser and E.Fedorovich. *Turbulence spectra and dissipation rates in a wind tunnel model of the atmospheric convective boundary layer*, J. Atmos. Sci. 55 (1998), pp. 580-594.

[4] D.K.Lilly. *On the numerical simulation of buoyant convection*, Tellus. 14 (1962), pp. 148-172.

[5] J.W.Deardorff. *On the magnitude of the subgrid scale eddy coefficient*, J. Comp Phys. 7 (1971), pp. 120-133.

[6] J.W.Deardorff. *Numerical investigation of neutral and unstable planetary boundary layers*, J. Atmos. Sci. 29 (1972), pp. 91-115.

[7] J.Smagorinsky. *General circulation experiments with the primitive equations*, Monthly Weather Review, 91 (1963), pp. 99-164.

[8] D.K.Lilly. *The representation of small-scale turbulence in numerical simulation experiments*, Proc. IBM Scientific Computing Symp on Environmental Sciences, Thomas J. Watson Research Center, Yorktown Heights, (1967), pp. 195-210.

[9] J.W.Deardorff. *Stratocumulus-capped mixed layers derived from a three-dimensional model*, Bound-Layer Meteor. 18 (1980), pp. 495-527.

[10] C.H.Moeng. *A large-eddy simulation model for the study of planetary boundary-layer turbulence*, J. Atmos. Sci. 41 (1984), pp. 2052-2062.

[11] J.W.Deardorff. *The use of subgrid transport equations in a three-dimensional model of atmospheric turbulence*, J. Fluids Eng., 95 (1973), pp. 429-438.

[12] J.W.Deardorff. *Three dimensional numerical study of turbulence in an entraining mixed layer*, Bound-Layer Meteor. 7 (1974), pp. 199-226.

[13] C.H.Moeng and J.C.Wyngaard. *Spectral analysis of large-eddy simulations of the convective boundary layer*, J. Atmos. Sci. 45 (1988), pp. 3573-3587.

[14] P.P.Sullivan and E.G.Patton. *The effect of mesh resolution on convective boundary layer statistics and structures generated by large-eddy simulation*, J. Atmos. Sci. 68 (2011), pp. 2395-2415.

[15] J.C.Wyngaard, *Turbulence in the Atmosphere*, Cambridge University Press, New York, NY, 2010. pp. 348-349.

[16] P.Mestayer. *Local isotropy and anisotropy in a high-Reynolds-number turbulent boundary layer*, J. Fluid Mech. 125 (1982), pp. 475-503.

[17] D.H.Lenschow *Airplane measurements of planetary boundary layer structure*, J. Appl. Meteor. 9 (1970), pp. 874-884.

[18] S.J.Caughey and S.G.Palmer. *Some aspects of turbulence through the depth of the convective boundary layer*, Quart. J. R. Met. Soc. 105 (1979), pp. 811-827.

[19] J.C.Kaimal and R.A.Eversole. *Spectral characteristics of the convective boundary layer over uneven terrain*, J. Atmos. Sci. 39 (1982), pp. 1098-1114.

[20] R.J.Grossman. *An analysis of vertical velocity spectra obtained in the Bomex fair-weather, trade-wind boundary layer*, Boundary-Layer Meteor. 23 (1982), pp. 323-357.

[21] J.W.Deardorff and G.E.Willis. *Further results from a laboratory model of the convective planetary boundary layer*, Bound-Layer Meteor. 32 (1985), pp. 205-236.

[22] F.T.M.Niewstadt, P.J.Mason, C.H.Moeng, and U.Schumann. *Large-eddy simulation of the convective boundary layer: A comparison of four computer codes*, Durst et al. (eds.), Turbulent Shear Flows, 8 (1993), pp. 343-367

[23] T.Takemi and R.Rotunno. *The effects of subgrid model mixing and numerical filtering in simulations of mesoscale cloud systems*, Monthly Weather Review, 131 (2003), pp. 2085-2101.

[24] E.Fedorovich. *Entrainment into sheared convective boundary layers as predicted by different large eddy simulation codes*, Preprints, 16th Symp. on Boundary Layers and Turbulence, Portland, ME, Amer. Meteor. Soc. (2004), P4.7.

[25] H-Y.Huang, B.Stevens, and S.A.Margulis. *Application of dynamic subgrid-scale models for large-eddy simulation of the daytime convective boundary layer over heterogeneous surfaces*, Bound-Layer Meteor. (2008), pp. 327-348.

[26] C.H.Moeng and P.P.Sullivan. *A comparison of shear and buoyancy driven planetary boundary layer flows*, J. Atmos. Sci. 51 (1994), pp. 999-1022.

[27] J.N.Koshyk and K.Hamilton. *The horizontal kinetic energy spectrum and spectral budget simulated by a high-resolution troposphere-stratosphere-mesoshpere GCM*, J. Atmos. Sci. 58 (2001), pp. 329-348.

[28] X.Capet, J.C.McWilliams, M.J.Molemaker, and A.F.Shchepetkin. *Mesoscale to submesoscale transition in the California current system. Part III: Energy balance and flux*, J. Phys. Ocean. 38 (2008), pp. 2256-2269.

[29] G.K.Vallis, *Atmospheric and Ocean Fluid Dynamics. Fundamentals and Large-Scale Circulation*, Cambridge University Press, New York, NY, 2006. pp. 73-77.

[30] S.B.Pope, *Turbulent Flows*, Cambridge University Press, New York, NY, 2000. pp 558-639.

[31] P.J.Mason. *Large-eddy simulation of the convective atmospheric boundary layer*, J. Atmos. Sci. 46 (1989), pp. 1492-1516.

[32] B.Stevens, C.H.Moeng, and P.P.Sullivan. *Large-eddy simulations of radiatively driven convection: Sensitivities to the representation of small scales*, J. Atmos. Sci. 56 (1999), pp. 3963-3984.

[33] D.R.Durran, *Numerical Methods for Fluid Dynamics: With Applications to Geophysics 2nd Edition*, Springer, New York, NY, 2010. pp. 146-157.

[34] A.J.Chorin. *Numerical solution of the Navier-Stokes equations*, Math. Comp., 22 (1968), pp. 745-762.
[35] R.V.Driel and H.J.J.Jonker. *Convective boundary layers driven by nonstationary surface heat fluxes*,
     J. Atmos. Sci. 60 (2011), pp. 727-738.
[36] M.L.Waite and C.Snyder. *The mesoscale kinetic energy spectrum of a baroclinic life cycle*, J. Atmos.
     Sci. 66 (2009), pp. 883-901.
[37] G.K.Vallis, G.J.Shutts, and M.E.B.Gray. *Balanced mesoscale motion and stratified turbulence forced
     by convection*, Q. J. R. Meteor. Soc. 123 (1996), pp. 1621-1652.
[38] P.A.Davidson, *Turbulence: An Introduction for Scientists and Engineers*, Oxford University Press,
     New York, NY, 2004. pp. 558-639.
[39] J.A.Gibbs and E.Fedorovich. *Comparison of convective boundary layer velocity spectra retrieved from
     large-eddy-simulation and weather research and forecasting model data*, J. Atmos. Sci. 53 (2014), pp.
     377-394.
[40] M.P.Kirkpatrick, A.S.Ackerman, D.E.Stevens, and N.N.Mansour. *On the application of the dynamic
     Smagorinsky model to large-eddy simulations of the cloud-topped atmospheric boundary layer*, J.
     Atmos. Sci. 63 (2006), pp. 526-546.
[41] P.J.Mason and A.R.Brown. *On subgrid models and filter operations in large eddy simulations*, J.
     Atmos. Sci. 56 (1999), pp. 2101-2114.
[42] H.J.J.Jonker, P.G.Duynkerke, and J.W.M.Cuijpers. *Mesoscale fluctuations in scalars generated by
     boundary layer convection*, J. Atmos. Sci. 56 (1999), pp. 801-808.
[43] S.R.De Roode, P.G.Duynkerke, and H.J.J.Jonker. *Large-eddy simulation: how large is large enough?*,
     J. Atmos. Sci. 61 (2004), pp. 403-421.

Appendix A.

In an unbounded domain, the horizontal wavenumber spectra of vertical and horizontal kinetic energy are defined as:

$$E_v(k_h) = \int_0^\infty \int_0^{2\pi} \frac{1}{2}\phi_{33}k_h d\theta dk_z \quad E_h(k_h) = \int_0^\infty \int_0^{2\pi} \frac{1}{2}(\phi_{11}+\phi_{22})k_h d\theta dk_z,$$
(A1)

where integration is over a cylinder in wavenumber space centred on the k_z axis with radius k_h. We assume the spectral tensor, ϕ_{ij}, has the usual isotropic form (e.g. [30]):

$$\phi_{ij} = \frac{E(k)}{4\pi k^2}\left(\delta_{ij} - \frac{k_i k_j}{k^2}\right),$$
(A2)

where $k = \sqrt{k_x^2 + k_y^2 + k_z^2}$. Substituting (A2) into (A1) yields:

$$E_v = \frac{1}{4}\int_0^\infty \frac{E(k)}{k^2}(\frac{k_h^2}{k^2})k_h dk_z \quad E_h = \frac{1}{4}\int_0^\infty \frac{E(k)}{k^2}(\frac{k_h^2 + 2k_z^2}{k^2})k_h dk_z.$$

Using $k_z^2 = k^2 - k_h^2$, the substitution $\eta = k/k_h$, and assuming a Kolmogorov energy spectrum $E(k) = \alpha\epsilon^{2/3}k^{-5/3}$, the above integrals can be reduced to:

$$E_v = \frac{1}{4}\alpha\epsilon^{2/3}k_h^{-5/3}\int_1^\infty \frac{\eta^{-14/3}}{\sqrt{\eta^2 - 1}}d\eta$$

$$E_h = \frac{1}{4}\alpha\epsilon^{2/3}k_h^{-5/3}\int_1^\infty \frac{(2\eta^2 - 1)\eta^{-14/3}}{\sqrt{\eta^2 - 1}}d\eta.$$

These integrals can be numerically evaluated give a vertical-to-horizontal ratio:

$$\frac{E_v}{E_h} \approx \frac{0.611861}{1.07075} \approx 0.5714.$$